The Compensator Approach: Solving the Transient Stability Issues of Virtual Synchronous Machines

The Compensator Approach: Solving the Transient Stability Issues of Virtual Synchronous Machines

Alessia Camboni, *Student Member IEEE*, Vincenzo Mallemaci, *Student Member IEEE*, Fabio Mandrile, *Member IEEE*, and Radu Bojoi, *Fellow IEEE*

***Abstract*—The continuous integration of renewable energy sources (RES) into the grid through power electronics impacts the power system stability, posing new challenges for control techniques implemented on power converters. The Virtual Synchronous Machine (VSM) represents a viable power converter control solution for the RES integration, providing natural grid support capability resulting from the emulation of the synchronous machine behaviour. However, the VSM control faces transient stability issues under large voltage sags due to the significant acceleration of the virtual rotor. The literature reports numerous transient stability analyses, proposing different control solutions to improve the transient response of Virtual Synchronous Generators (VSGs). However, they increase the complexity of the control algorithm, requiring additional tuning. Furthermore, they often mitigate rather than eliminate the transient stability issues. Therefore, this paper provides a new perspective on VSM implementation, proposing the Virtual Synchronous Compensator (VSC) concept as a straightforward and definitive solution to eliminate the VSM's transient instability. The VSC maintains its synchronism under large and prolonged voltage sags, overcoming the transient stability issues implied by conventional VSG algorithms without additional control modules. The VSC's transient response is verified theoretically and experimentally, proving the claimed benefits.**

***Index Terms*—Power electronic interface for power generation, Virtual Synchronous Machines, Transient Stability.**

I. Introduction

In modern power systems, the integration of renewable energy sources (RES) has faced a significant increase during the last decade. Several RES, such as photovoltaic and wind sources, interface to the grid through power converters. However, the interaction between RES and the grid revolves around the control approach implemented on the power converter level, thus impacting the power system's reliability (i.e., lack of inertia and fault ride-through capability [1]–[4]). The Virtual Synchronous Machine (VSM) control enables power converters to provide ancillary services to the grid by mimicking the synchronous machines' (SMs) behaviour. For instance, VSM control reduces the Rate of Change of Frequency (RoCoF) [1]–[8] thanks to its inertial dynamic [1], [2], [5], [6]. Furthermore, the excitation control injects reactive power, supporting the grid during faults [7], [8]. Therefore, VSMs represent a promising solution in the RESs' integration, improving the power system's stability [6], [7].

Several VSM solutions are proposed in the literature. The majority of them operate as Virtual Synchronous Generator (VSG), regulating the power exchange to the grid through mechanical and excitation control emulations. However, the mimicking of Synchronous Generators (SGs) implies transient stability issues during large disturbances [9]. The imbalance between the required active power and the transmissible one determines a significant acceleration of the virtual rotor, with possible loss of synchronism. Therefore, the study of VSM's transient stability has assumed a central role in the RES's integration challenges.

The literature provides numerous transient stability models and analyses for traditional SMs [9]–[12], re-elaborating them for modern VSMs [13]–[15]. Nevertheless, some of the proposed approaches rely on too restrictive assumptions. For instance, the authors in [13] consider the Equal Area Criteria (EAC), a suitable approach only for constant transmissible power during the fault [9], [10]. On the other hand, the authors in [16] carry out a more extensive stability analysis but without including the excitation control dynamic. A more in-depth study is provided in [14], pointing out the effect of the excitation control on the VSM's transient response. Nevertheless, the available papers focus on VSMs operating as VSGs, which exhibit transient stability issues. Therefore, these studies propose control modifications to improve the transient stability (i.e., power reference variation [14], [17], inertia adaptation [18], [19], and virtual impedance variation [20]). The baseline VSG algorithm is indeed modified to mitigate the transient stability issue, thus increasing the complexity of the control.

However, the VSG control does not represent the only VSM-based solution that provides ancillary services to the grid. The VSM can indeed operate as a Virtual Synchronous Compensator (VSC) [8]. In this case, the control incorporates two components: a traditional inverter control structure responsible for power exchange to the grid and a VSM component dedicated to providing grid services. This configuration enables the converter to exchange power with the rapid dynamic of a conventional control while simultaneously

Alessia Camboni, Vincenzo Mallemaci, Fabio Mandrile and Radu Bojoi are with the Dipartimento Energia "G. Ferraris", Politecnico di Torino, Torino, 10129, Italy (e-mail: alessia.camboni@polito.it).

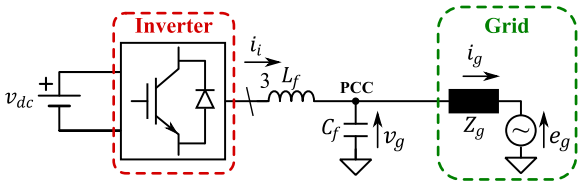

Fig. 1. Schematic overview of a grid-tied inverter.

offering ancillary services [8]. Furthermore, the VSC operates at zero power reference for the mechanical emulation of SMs, thus improving the transient stability without requiring dedicated control units. Nevertheless, the available studies do not explore the VSC mode, not considering a more straightforward solution to enhance the VSM's transient stability.

Therefore, the paper main contribution is to demonstrate, theoretically and experimentally, the immunity of the VSC approach to transient stability issues. For this purpose, the paper provides a comprehensive transient stability analysis based on Lyapunov's Direct Method. The proposed stability analysis is experimentally validated, proving the remarkable transient stability improvement obtained with the VSC.
The VSC control indeed overcomes the limitation of the VSG solutions available in the literature and features the following advantages:

- No loss of synchronism during large and prolonged voltage sags, hence no transient stability issues;
- The same control scheme is used for normal and abnormal conditions;
- No fault detection algorithm is required;
- No parameter variation or tuning is needed.

The paper is organized as follows. Section II recalls the VSM model, deriving the equivalent circuit and the mathematical model needed for the stability analysis formulation. Section III describes Lyapunov's direct method. In Section IV, the transient stability analysis is then experimentally validated for VSG and VSC controls. Finally, Section V concludes the paper.

II. Virtual Synchronous Machine Model

The system under study, illustrated in Fig. 1, consists of a three-phase inverter connected to the grid through an LC filter. The grid is represented as a voltage source e_{g} in series with its line impedance $\bar{Z}_{\mathrm{g}} = R_{\mathrm{g}} + jL_{\mathrm{g}}$. Fig. 2a shows the overall VSM control scheme, which combines the Electromechanical (EM) emulation with a parallel power injection of P_{set} and Q_{set} [8].

The VSM algorithm employs a current regulator to control the inverter current through the voltage reference v^* according to the reference current i_{i}^*. As illustrated in Fig. 2a, the reference current i_{i}^* consists of the sum of two contributions: the virtual current reference i_{v} from the EM emulation and the set point reference current i_{set}, which results from the Power to Current block.

This control architecture can operate as VSG and VSC [8]. A higher control level (e.g., Maximum Power Point Tracking (MPPT), droop control) defines the power references P^* and

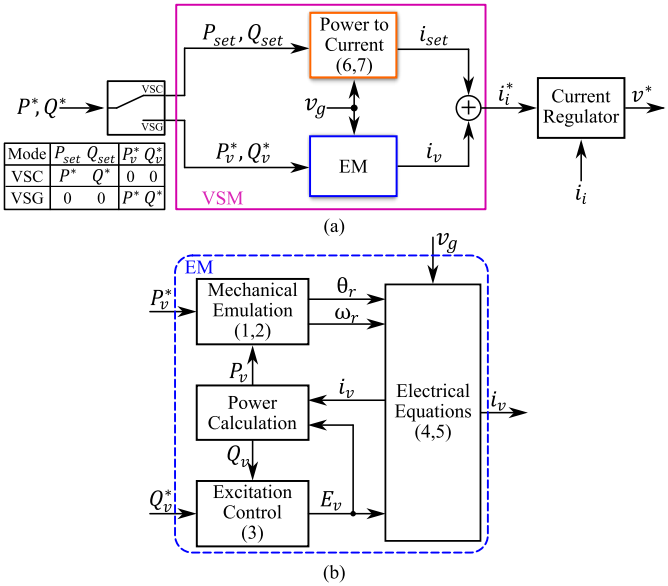

Fig. 2. (a) VSM control in VSG mode and VSC mode, (b) EM emulation of VSM.

Q^*, which are applied to the EM part in VSG mode or Power to Current block in VSC mode according to the selector in Fig. 2a.

Starting from the EM part in Fig. 2b, it emulates the dynamic of the SM via the swing equation (1) and the excitation control (3). The first one mimics the mechanical behaviour of an SM through the inertia constant H. Moreover, the implemented damping strategy consists of the droop-based damping. The coefficient D_{p} is tuned according to [21]. Eq. (1) defines the virtual rotor speed dynamic, which varies from the nominal grid angular speed ω_0 as $\omega_{\mathrm{r}} = \Delta\omega_{\mathrm{r}} + \omega_0$. Furthermore, the rotor angle θ_{r} is derived from ω_{r} as in (2). The excitation control (3) sets the dynamic of the electromotive force amplitude $E_{\mathrm{v}} = \Delta E_{\mathrm{v}} + E_{\mathrm{v0}}$ with the time constant T_{e} and the gain integral k_{e}, tuned according to [22].

$$P_{\mathrm{v}}^* - P_{\mathrm{v}} = 2H\frac{d\Delta\omega_{\mathrm{r}}}{dt} + D_{\mathrm{p}}\Delta\omega_{\mathrm{r}} \tag{1}$$

$$\frac{d\theta_{\mathrm{r}}}{dt} = \Delta\omega_{\mathrm{r}} + \omega_0 \tag{2}$$

$$Q_{\mathrm{v}}^* - Q_{\mathrm{v}} = \frac{T_{\mathrm{e}}}{\omega_{\mathrm{r}} k_{\mathrm{e}}}\frac{d\Delta E_{\mathrm{v}}}{dt} \tag{3}$$

The EM control indeed emulates the electromotive force e_{v} via the electrical relations (4) and (5) in the synchronous reference frame (d, q), where the $\bar{Z}_v = R_v + jL_v$ represents the virtual impedance. Moreover, the output of the EM control block is the virtual current i_{v}, which is sent to the current regulator. Therefore, the EM emulation can be represented as a controlled current source, as illustrated in Fig. 3.

$$e_{\mathrm{v,d}} - v_{\mathrm{g,d}} = R_{\mathrm{v}} i_{\mathrm{v,d}} - \omega_{\mathrm{r}} L_{\mathrm{v}} i_{\mathrm{v,q}} + L_{\mathrm{v}}\frac{di_{\mathrm{v,d}}}{dt} \tag{4}$$

$$e_{\mathrm{v,q}} - v_{\mathrm{g,q}} = R_{\mathrm{v}} i_{\mathrm{v,q}} + \omega_{\mathrm{r}} L_{\mathrm{v}} i_{\mathrm{v,d}} + L_{\mathrm{v}}\frac{di_{\mathrm{v,q}}}{dt} \tag{5}$$

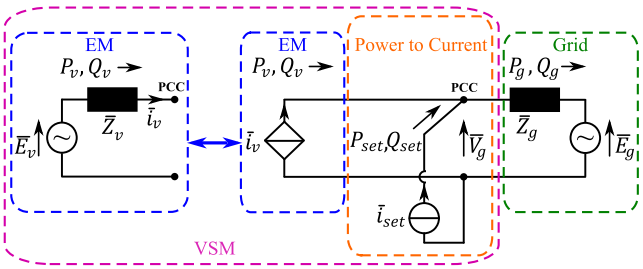

Fig. 3. Equivalent circuit of a grid-tied inverter with the VSM control.

A. VSM Operating Modes: VSG versus VSC

When operating as VSG, the parallel power injection does not act (i.e., $(P_{\text{set}}, Q_{\text{set}}) = 0$), and the term i_{set} is consequently equal to zero. Thus, the EM control is in charge of managing the power exchange to the grid according to the power references $P_{\text{v}}^* = P^*$ and $Q_{\text{v}}^* = Q^*$ through the term i_{v}. Therefore, the output power follows the slow dynamic of the mechanical emulation and excitation control.

On the other hand, the VSC control operates through the sum of the two terms i_{set} and i_{v}. As shown in Fig. 2a, the power references P^* and Q^* are applied to the Power to Current block (i.e., $P_{\text{set}} = P^*$ and $Q_{\text{set}} = Q^*$), whereas the virtual power references P_{v}^* and Q_{v}^* are equal to zero. Therefore, in steady state operation, i_{set} executes the power exchange to the grid, while i_{v} is equal to zero. Moreover, the VSC responds dynamically to the power system perturbations thanks to the virtual current reference i_{v} (i.e., the EM's output). Therefore, the VSC structure is able to provide ancillary services to the grid (e.g., inertial behaviour, reactive current during faults) [8]. In VSC mode, the current references in dq-frame $i_{\text{set,d}}, i_{\text{set,q}}$ are calculated from P_{set} and Q_{set}, as expressed in (6) and (7) according to [8]. The injection of P_{set} and Q_{set} takes place with a faster dynamic than P_{v}^* and Q_{v}^*, being directly injected from the inner current controller.

$$i_{\text{set,d}} = \frac{P_{\text{set}} v_{\text{g,d}} + Q_{\text{set}} v_{\text{g,q}}}{v_{\text{g,d}}^2 + v_{\text{g,q}}^2} \tag{6}$$

$$i_{\text{set,q}} = \frac{P_{\text{set}} v_{\text{g,q}} - Q_{\text{set}} v_{\text{g,d}}}{v_{\text{g,d}}^2 + v_{\text{g,q}}^2} \tag{7}$$

B. Equivalent Circuit and Dynamic Model

This subsection presents the equivalent circuit of the VSM control shown in Fig. 2. Based on the equivalent circuit, the VSM dynamic model is then derived to perform the transient stability analysis.

For the sake of simplicity, the following assumptions have been considered:

- The current controller is assumed to be ideal, being fast enough and thereby not affecting the VSM's outer control loops (i.e., $i_{\text{i}} \approx i_{\text{i}}^*$);
- The effect of the filter capacitor C_f is neglected (i.e., $i_{\text{i}} \approx i_{\text{g}}$).

Therefore, the VSM equivalent circuit results as in Fig. 3, where the EM and Power to Current block equivalents operate in parallel. Starting from the EM part, the controlled current source behaves as an equivalent Thevenin circuit. Indeed, the virtual current i_{v} follows the electrical relations (4) and (5). Therefore, the EM block in Fig. 2 is modelled as the equivalent Thevenin circuit, consisting of an ideal voltage source $\bar{E}_{\text{v}}$ in series with its impedance $\bar{Z}_{\text{v}}$, as shown in Fig. 3. The swing equation (1) and excitation control (3) vary the electromotive force in phase and amplitude, leading to the power exchange P_{v} and Q_{v} with the point of common coupling (PCC). On the other hand, a current source in parallel to the PCC represents the power injection of P_{set} and Q_{set}. Note that the current injection is immediate, assuming that $i_{\text{i}} \approx i_{\text{i}}^*$.

From the equivalent circuit in Fig. 3, the system is described by a set of differential and algebraic equations for the theoretical analysis. The swing equation (1) and excitation control (3) rule the system dynamic, identifying the state variables as $x = [\Delta\delta \quad \Delta\omega_{\text{r}} \quad \Delta E_{\text{v}}]$. Eq. (8) summarizes the differential equations, where $\delta = \Delta\delta + \delta_0$ is the phase-shift between the electromotive force $\bar{E}_{\text{v}}$ and the grid voltage $\bar{E}_{\text{g}}$.

$$\begin{cases} \dfrac{d\Delta\delta}{dt} = \Delta\dot{\delta} = \Delta\omega_{\text{r}} \\ \dfrac{d\Delta\omega_{\text{r}}}{dt} = \Delta\dot{\omega}_{\text{r}} = \dfrac{1}{2H}(P_{\text{v}}^* - P_{\text{v}} - D_{\text{p}}\Delta\omega_{\text{r}}) \\ \dfrac{d\Delta E_{\text{v}}}{dt} = \Delta\dot{E}_{\text{v}} = \dfrac{k_{\text{e}}\omega_{\text{r}}}{T_{\text{e}}}(Q_{\text{v}}^* - Q_{\text{v}}) \end{cases} \tag{8}$$

The algebraic variables are the voltage amplitude and phase at the PCC, indicated as $y = [V_{\text{g}} \quad \phi_{\text{g}}]$, obtained by solving the active and reactive power balance equations at the PCC node. The active power balance equation is (9), where P_{loss} are the active power losses between $\bar{E}_{\text{v}}$ and $\bar{V}_{\text{g}}$ due to R_{v}, calculated as in (10) [23]. Moreover, the active power P_{v} is defined as in (11), whereas the term P_{g} is the active power exchanged between the PCC and the grid, expressed as in (12).

$$0 = (P_{\text{v}} - P_{\text{loss}}) + P_{\text{set}} - P_{\text{g}} \tag{9}$$

$$P_{\text{loss}} = R_{\text{v}} I_{\text{v}}^2 = \frac{R_{\text{v}}}{Z_{\text{v}}^2}\left(E_{\text{v}}^2 + V_{\text{g}}^2 - 2E_{\text{v}}V_{\text{g}}\cos(\delta - \phi_{\text{g}})\right) \tag{10}$$

$$P_{\text{v}} = \frac{R_{\text{v}}}{Z_{\text{v}}^2}E_{\text{v}}^2 + \frac{L_{\text{v}}}{Z_{\text{v}}^2}E_{\text{v}}V_{\text{g}}\sin(\delta - \phi_{\text{g}}) - \frac{R_{\text{v}}}{Z_{\text{v}}^2}E_{\text{v}}V_{\text{g}}\cos(\delta - \phi_{\text{g}}) \tag{11}$$

$$P_{\text{g}} = \frac{R_{\text{g}}}{Z_{\text{g}}^2}V_{\text{g}}^2 + \frac{L_{\text{g}}}{Z_{\text{g}}^2}V_{\text{g}}E_{\text{g}}\sin(\phi_{\text{g}}) - \frac{R_{\text{g}}}{Z_{\text{g}}^2}V_{\text{g}}E_{\text{g}}\cos(\phi_{\text{g}}) \tag{12}$$

The reactive power balance equation is described by (13), where Q_{v} and Q_{g} are expressed as in (14) and (15), respectively.

$$0 = Q_{\text{v}} + Q_{\text{set}} - Q_{\text{g}} \tag{13}$$

$$Q_{\text{v}} = \frac{L_{\text{v}}}{Z_{\text{v}}^2}E_{\text{v}}^2 - \frac{L_{\text{v}}}{Z_{\text{v}}^2}E_{\text{v}}V_{\text{g}}\cos(\delta - \phi_{\text{g}}) - \frac{R_{\text{v}}}{Z_{\text{v}}^2}E_{\text{v}}V_{\text{g}}\sin(\delta - \phi_{\text{g}}) \tag{14}$$

$$Q_{\text{g}} = \frac{L_{\text{g}}}{Z_{\text{g}}^2}V_{\text{g}}^2 - \frac{L_{\text{g}}}{Z_{\text{g}}^2}V_{\text{g}}E_{\text{g}}\cos(\phi_{\text{g}}) - \frac{R_{\text{g}}}{Z_{\text{g}}^2}V_{\text{g}}E_{\text{g}}\sin(\phi_{\text{g}}) \tag{15}$$

The expressions for P_{v} can be modified as in (16) utilizing the admittance matrix $\mathbf{Y} = \mathbf{G} + j\mathbf{B}$ between the VSM and the grid. The admittance matrix considers the equivalent circuit in Fig. 3. Therefore, $\mathbf{G}$ and $\mathbf{B}$ depend on the virtual impedance $\bar{Z}_{\text{v}}$, grid impedance $\bar{Z}_{\text{g}}$, and a negative load, which represents

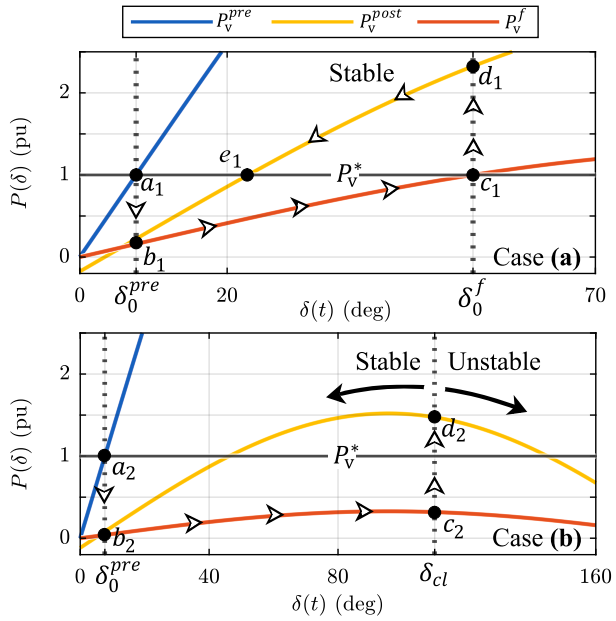

Fig. 4. Examples of system trajectory during a large voltage sag: stable (a) and unstable (b) cases. The different power-angle curves are: pre-fault $P_v^{pre}(\delta)$ in blue, fault $P_v^f(\delta)$ in orange, and post-fault $P_v^{post}(\delta)$ in yellow.

the power injection of P_{set} and Q_{set} at the PCC [10]. For a detailed description of **G** and **B** refer to the Appendix.

$$P_v = G_{11}E_v^2 + B_{12}E_vE_g\sin(\delta) + G_{12}E_vE_g\cos(\delta) \quad (16)$$

III. Transient Stability Analysis with Lyapunov's Direct Method

This section describes a transient stability evaluation method for the VSM-based control. For this purpose, the underlying transient stability mechanism of a VSM is qualitatively described by observing the virtual angle trajectory in the power-angle characteristic.

Let's consider a scenario where the VSM operates as VSG (i.e., $P_v^* \neq 0, P_{set} = 0$) with zero reactive power reference. The stationary conditions of (8) define the equilibrium points in the pre-fault state. Similarly, the intersection of the power-angle characteristic and the active power reference identifies the stable δ_0^{pre} equilibrium point, as shown graphically in Fig. 4. During a symmetrical voltage sag, two main scenarios can occur: **(a)** the fault characteristic $P_v^f(\delta)$ still presents a stable equilibrium point; **(b)** $P_v^f(\delta)$ does not present a stable equilibrium point.

In case **(a)**, the virtual rotor accelerates along the fault characteristic until reaching the stable equilibrium point c_1, where it settles for the remaining fault period, as depicted in Fig. 4. The system will be stable in post-fault if a stable equilibrium point exists in the post-fault condition. In this example, the system features a stable equilibrium point in post-fault, indicated as e_1 in Fig. 4a.

For case **(b)**, the virtual rotor continues to accelerate and moves along the power-angle fault characteristic $P_v^f(\delta)$ until the fault is cleared at δ_{cl}, as illustrated in Fig. 4. Then, the virtual rotor follows the post-fault characteristic $P_v^{post}(\delta)$. In this condition, the system can either move to the unstable part of the power-angle curve or return to the pre-fault state. The system dynamic in the post-fault state depends on the energy accumulated during the fault and the potential energy's capability to lead the system back to the pre-fault state.

As it emerges from these qualitative considerations, a more thorough analysis is necessary to assess the system's stability. For this purpose, this paper adopts the Lyapunov's direct method to estimate the clearing time after which the system is unstable, also called critical clearing time t_{cr} [9], [24]. In contrast to the EAC [11], this method can also be applied in the case of variable $P_v^f(\delta)$ [9], [10]. The Lyapunov's direct method is therefore discussed in the following subsection.

A. Lyapunov's Direct method

The Lyapunov's direct method utilizes a generic Lyapunov's function, which is the energy function $W(t)$, traditionally adopted for the study of SMs system [9]. Based on the energy concept, Lyapunov's direct method evolves into the following transient stability assessment. The stability evaluation revolves around the comparison of two energy function values observing the last instant of the disturbance [9]:

- The energy function at the clearing time t_{cl} of the fault, indicated as $W_{cl} = W(t_{cl})$;
- The critical energy value W_{cr} is the value of $W(t)$ at the unstable equilibrium point for the given post-fault condition.

If $W_{cl} < W_{cr}$, the system will be stable in the post-fault condition, whereas if $W_{cl} > W_{cr}$, it will be unstable in the post-fault condition. Moreover, the clearing time for which $W_{cl} = W_{cr}$ identifies the critical clearing time t_{cr}. Therefore, t_{cr} represents the clearing time after which the system is unstable in post-fault.

Note that the transient stability assessment based on the energy function is not general but depends on the pre-fault, fault, and post-fault conditions. This paper applies the Lyapunov's method for a three-phase symmetrical voltage dip. For an asymmetrical fault, the analysis can be applied separately to the positive sequence, while the negative sequence causes a zero average oscillation in the total system response.

1) Energy Function: The energy function, indicated as $W(t)$, is the sum of the kinetic $(W_{KE}(t))$ and the potential energy $(W_{PE}(t))$ of the dynamic system. When considering the damping factor in the swing equation (1), $W(t)$ includes an additional term for the mechanical energy losses due to the movement of the virtual rotor, indicated as $W_D(t)$. Therefore, the general formulation is given by (17).

$$W(t) = W_{KE}(t) + W_{PE}(t) + W_D(t) \quad (17)$$

The energy function can be written in terms of state variables as $W(x) = W(x(t))$, implying the dependence on the time. The kinetic energy W_{KE} depends on the virtual rotor speed variation $\Delta\omega_r$, as written in (18), where $M = {}^{2H}/_{\omega_0}$.

$$W_{KE}(x) = W_{KE}(\Delta\omega_r) = \frac{1}{2}M\Delta\omega_r^2 \quad (18)$$

The potential energy of the system W_{PE} depends on the difference between the transmissible power and the active

power reference, as expressed in (19) [9]. As derived in Section II-B, the active power $P_{\rm v}$ depends on δ and $E_{\rm v}$, generally referred to as $P_{\rm v}(x)$.

$$W_{\rm PE}(\delta) = \int_{\delta_0^{pre}}^{\delta} \left(P_{\rm v}(x) - P_{\rm v}^{*}\right) d\alpha \tag{19}$$

According to [9], the energy losses $W_{\rm D}$ due to the mechanical damping are defined as in (20).

$$W_{\rm D}(\delta) = \int_{\delta_0^{pre}}^{\delta} D_{\rm p} \Delta\omega_{\rm r} d\alpha \tag{20}$$

The potential energy and damping energy losses are further analyzed in the next subsections.

2) Potential Energy: The potential energy represents the capability of the system to increase or reduce its speed, moving toward the unstable or stable area in the $(P-\delta)$ frame. Therefore, $W_{\rm PE}$ depends on the VSM transmissible power $P_{\rm v}$ [9]. When considering the excitation control (8), the active power, in turn, is a function of the two state variables $E_{\rm v}$ and δ. However, it is not possible to analytically express $P_{\rm v}$ as only δ-dependent to solve the integral in (19) [9], [14], [25]. Therefore, a common approximation is to assume $E_{\rm v}$ as a constant inside the potential energy integral, meaning $dE_{\rm v}/d\delta = 0$ [9]. Under this assumption, the potential energy is calculated as in (21).

$$\begin{aligned} W_{\rm PE}(\delta) &= \left(G_{11}E_{\rm v}^2 - P_{\rm v}^{*}\right)(\delta - \delta_0^{pre}) \\ &- B_{12}E_{\rm v}E_{\rm g}\cos(\delta - \delta_0^{pre}) + G_{12}E_{\rm v}E_{\rm g}\sin(\delta - \delta_0^{pre}) \end{aligned} \tag{21}$$

3) Damping Factor Effect: The energy losses due to the mechanical damping depend on the virtual rotor speed, as expressed in (20). By replacing (8) in (20), the term $W_{\rm D}$ can be written as in (22). The obtained equation does not feature an analytical solution, being linearly dependent on the trajectory of the state variable during the fault. Numerous approximations for the state variables trajectory are available in the literature [9], [26]. Despite this, assuming negligible energy losses leads to a more conservative estimation of the critical clearing time $t_{\rm cr}$ [27]. Therefore, the term $W_{\rm D}$ is not further considered in the analysis, accepting a conservative estimation error for $t_{\rm cr}$.

$$W_{\rm D}(\delta) = \int_{\delta_0^{pre}}^{\delta} \left(D_{\rm p}\frac{d\alpha}{dt}\right) d\alpha \tag{22}$$

4) Energy Function Clearing Value: The transient stability assessment states that $W_{\rm cl}$ is the energy function value at the clearing time. Therefore, $W_{\rm cl}$ is identified by applying its definition. The energy value $W_{\rm cl}$ is obtained by combining (18) and (21) as follows:

$$W_{\rm cl} = W_{\rm KE}(\Delta\omega_{\rm r,cl}) + W_{\rm PE}(\delta_{\rm cl}, \Delta E_{\rm v,cl}) \tag{23}$$

where $\delta_{\rm cl} = \delta(t_{\rm cl})$, $\Delta\omega_{\rm r,cl} = \Delta\omega_{\rm r}(t_{\rm cl})$, $\Delta E_{\rm v,cl} = \Delta E_{\rm v}(t_{\rm cl})$ are the state variables at the clearing time $t_{\rm cl}$.

5) Energy Function Critical Value: The critical value $W_{\rm cr}$ is the system energy at the unstable equilibrium point in post-fault, indicated as $\delta_{\rm max}^{post}$. Being $\delta_{\rm max}^{post}$ an equilibrium point, the stationary conditions (24) are met. Note that the angular stationary condition leads to zero kinetic energy (i.e., $\Delta\dot{\delta} = 0 \Rightarrow \Delta\omega_{\rm r} = 0 \Rightarrow W_{\rm KE,cr} = 0$).

$$\Delta\dot{\delta} = 0, \quad \Delta\dot{\omega}_{\rm r} = 0 \tag{24}$$

However, the unstable equilibrium state does not imply the electromotive force stationary condition if considering the excitation control dynamic (i.e., $\Delta\dot{E}_{\rm v} \neq 0$) [25]. Therefore, the proposed approach to identify the critical value $W_{\rm cr}$ is the following:

- Assume knowing numerically $E_{\rm v}$ in the post-fault, named $\underline{E}_{\rm v}^{post}$;
- $\underline{E}_{\rm v}^{post}$ is a numerical vector, where the i-th term $E_{\rm v,i}^{post}$ is $E_{\rm v,i}^{post} = \underline{E}_{\rm v}^{post}(t_{\rm i})$ with $t_{\rm i} > t_{\rm cl}$;
- The unstable equilibrium point $\delta_{\rm max,i}^{post}$ is calculated locally for each value of $E_{\rm v,i}^{post}$ by imposing (24), obtaining the numerical vector $\underline{\delta}_{\rm max}^{post}$;
- For each pair $[\delta_{\rm max,i}^{post},\ E_{\rm v,i}^{post}]$, the local critical energy is defined as $W_{\rm cr,i} = W_{\rm PE}(\delta_{\rm max,i}^{post}, E_{\rm v,i}^{post})$, according to (21);
- By calculating $W_{\rm cr,i}$ for each $t_{\rm i} > t_{\rm cl}$, the numerical vector $\underline{W}_{\rm cr}$ is defined in the post-fault period;
- The chosen critical value for the stability assessment is the minimum critical energy $W_{\rm cr}^{min}$, meaning a more conservative estimation of the critical clearing time.

The proposed approach is summarized in (25).

$$W_{\rm cr}^{min} = \min\left(\underline{W}_{\rm cr}\right) = \min\left(W_{\rm PE}(\underline{\delta}_{\rm max}^{post}, \underline{E}_{\rm v}^{post})\right) \tag{25}$$

Note that the energy function discussed so far does not include either the converter's limitations (e.g., current control saturation) or the energy source's limitations (e.g., electrochemical dynamics [28]). Indeed, the paper's main purpose is to highlight the fundamental differences between VSC and VSG operations while maintaining the generality of the analysis.

B. Numerical Implementation

The system dynamic is simulated in MATLAB through the differential and algebraic equations specified in Section II-B. Three time spans define the simulation's steps for the transient stability analysis:

1) **Pre-fault condition**: from the initial time t_0 to the fault time $t_{\rm f}$. In the pre-fault condition, the stable equilibrium point is calculated, defining the initial condition for the next time span;
2) **Fault condition**: when a symmetrical voltage sag is applied to the grid from the fault time $t_{\rm f}$ to the clearing time $t_{\rm cl}$;
3) **Post-fault condition**: after the fault is cleared at $t_{\rm cl}$.

The first step consists of calculating the stable equilibrium point in the pre-fault condition, thus meeting the following relations:

$$\Delta\dot{\delta}^{pre} = 0, \quad \Delta\dot{\omega}_{\rm r}^{pre} = 0, \quad \Delta\dot{E}_{\rm v}^{pre} = 0 \tag{26}$$

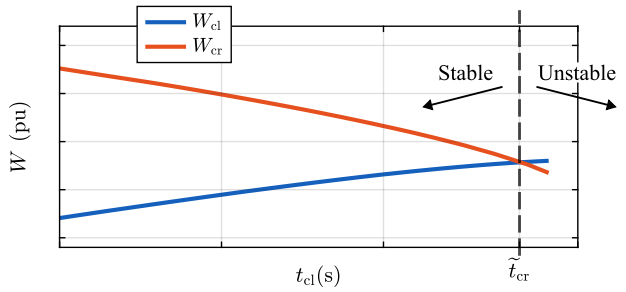

Fig. 5. Simulation example of critical $W_{\rm cr}$ and clearing $W_{\rm cl}$ values for a symmetrical voltage sag.

Replacing (26) in (8), (27) is derived.

$$\begin{cases} \Delta\dot{\delta}^{pre} & = 0 \;\Rightarrow\; \Delta\omega_{\rm r}^{pre} = 0 \\ \Delta\dot{\omega}_{\rm r}^{pre} & = 0,\; \Delta\omega_{\rm r}^{pre} = 0 \;\Rightarrow\; P_{\rm v} = P_{\rm v}^{*} \\ \Delta\dot{E}_{\rm v}^{pre} & = 0 \;\Rightarrow\; Q_{\rm v}^{pre} = Q_{\rm v}^{*} \end{cases} \tag{27}$$

Therefore, the algebraic equations can be written as follows:

$$0 = (P_{\rm v}^{*} - P_{\rm loss}^{pre}) + P_{\rm set} - P_{\rm g}^{pre} \tag{28}$$

$$0 = Q_{\rm v}^{*} + Q_{\rm set} - Q_{\rm g}^{pre} \tag{29}$$

The equations system consisting of (27), (28), and (29) is solved, thus obtaining the state and algebraic variables in pre-fault condition. Next, the fault is applied until $t_{\rm cl}$, at which the energy function value $W_{\rm cl}$ is calculated according to (23). After simulating the post-fault condition, the minimum critical energy value $W_{\rm cr}^{min}$ is computed according to Section III-A5. The described algorithm is repeated for different clearing times, obtaining the numeric values $W_{\rm cl}(t_{\rm cl})$ and $W_{\rm cr}^{min}(t_{\rm cl})$. Then, the critical clearing time $\widetilde{t}_{\rm cr}$ is estimated by comparing $W_{\rm cl}(t_{\rm cl})$ and $W_{\rm cr}^{min}(t_{\rm cl})$. Fig. 5 shows a simulation example of the clearing and critical energy values plotted to the variation of $t_{\rm cl}$ for a symmetrical voltage sag. The virtual rotor accelerates while the fault persists, thus increasing the energy $W_{\rm cl}$ with the clearing time. On the other hand, the critical energy decreases while the fault persists, meaning a lower potential energy to bring the system back to its stable point. The intersection between clearing and critical energy identifies the estimated critical clearing time $\widetilde{t}_{\rm cr}$. According to the stability assessment, the system is stable in post-fault if $t_{\rm cl} < \widetilde{t}_{\rm cr}$ whereas unstable if $t_{\rm cl} > \widetilde{t}_{\rm cr}$. From now on, $W_{\rm cr}$ refers to $W_{\rm cr}^{min}$ for simplicity.

IV. Experimental Validation

The system shown in Fig. 1 has been tested to evaluate its transient stability analysis, as discussed in the above sections. The assessment stated in Section III gives a general procedure, which is applied in two cases: the control operating as VSG and VSC. As presented in Section II, the VSG control applies the power references through the swing equation and excitation control (i.e.,$(P_{\rm v}^{*}, Q_{\rm v}^{*}) \neq 0$, and $(P_{\rm set}, Q_{\rm set}) = 0$). On the other hand, the current controller directly sets the power references during the VSC operation (i.e., $(P_{\rm set}, Q_{\rm set}) \neq 0$). In VSC mode, the VSM part operates at $P_{\rm v}^{*} = 0$, thus expecting to improve the transient stability. Therefore, these two control approaches are tested, observing their transient responses for the same fault conditions.

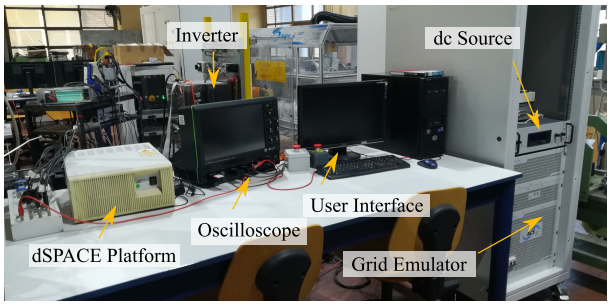

Fig. 6. Experimental setup.

TABLE I
Experimental Setup Parameters.

Inverter		Base Values		Grid	
$S_{\rm N}$	15 kVA	$S_{\rm base}$	1.5 kVA	$\widehat{V}_{\rm g}$	$120\sqrt{2}$ V
$I_{\rm N}$	60 A	$V_{\rm base}$	$120\sqrt{2}$ V	$L_{\rm g}$	0.037 pu
$f_{\rm sw}$	10 kHz	$\omega_{\rm base}$	314 rad/s V	$R_{\rm g}$	0.005 pu
VSM				**LC Filter**	
$L_{\rm v}$	0.1 pu	$D_{\rm p}$	232.4 pu	$L_{\rm f}$	0.006 pu
$R_{\rm v}$	0.02 pu	$T_{\rm e}$	1 s	$C_{\rm f}$	0.199 pu
H	6 s	$k_{\rm e}$	0.1368 pu		

A. Experimental Setup

The experimental setup is depicted in Fig. 6. A 15 kVA, two-level three-phase inverter is connected to a grid emulator through an LC filter and an additional impedance $Z_{\rm g}$. An ideal DC source supplies the inverter, which is controlled through the dSPACE platform. The considered base power $S_{\rm base}$ is 1.5 kVA, thus allowing not to trip the over-current protection during the fault and safely test the unstable conditions. Table I summarizes the main system and control parameters, tuned according to [6], [8].

B. Experimental Results

In pre-fault conditions, the VSG and VSC work at zero reactive power reference, while $P_{\rm v}^{*} = 1$ pu and $P_{\rm set} = 1$ pu, respectively. Then, a symmetrical voltage sag of -0.7 pu occurs at $t_{\rm f} = 1$ s. Moreover, the post-fault condition coincides with the complete restoration of the grid voltage, meaning $E_{\rm g}^{post} = E_{\rm g}^{pre}$. The experiment is repeated for several clearing times $t_{\rm cl}$. Next, the energy function values $W_{\rm cr}$ and $W_{\rm cl}$ are computed for each $t_{\rm cl}$ to estimate the critical clearing time $\widetilde{t}_{\rm cr}$.

VSG Results: Starting from the conventional VSG operation, Fig. 7 illustrates the energy values, $W_{\rm cr}$ and $W_{\rm cl}$, to the variation of $t_{\rm cl}$, obtained from the experimental tests and compared with the simulation ones. As shown in Fig. 7, the simulation and experimental results match well, thus validating the mathematical model presented in Section II-B. As expected from Sections III-A3 and III-A5, the approximations accepted for $W_{\rm D}$ and $W_{\rm cr}$ lead to a conservative estimation error. The tested system is indeed stable for $t_{\rm cl} = \widetilde{t}_{\rm cr} = 5.85$ s as shown in Fig. 8, namely a conservative estimation of $\widetilde{t}_{\rm cr}$. Therefore, the fault is applied for $t_{\rm cl} > \widetilde{t}_{\rm cr}$ and the actual critical clearing time $t_{\rm cr}$ results in 6.01 s. The VSG indeed reaches the unstable condition for $t_{\rm cl} = 6.01$ s, as shown in

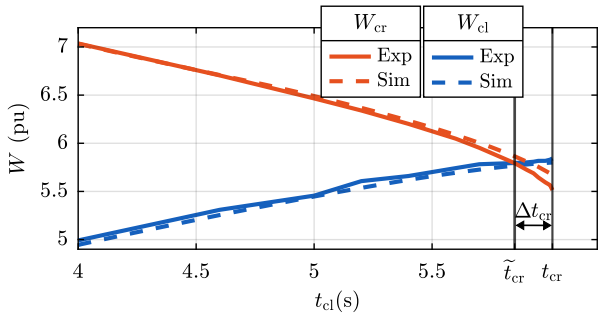

Fig. 7. Critical W_{cr} and clearing W_{cl} values for a symmetrical voltage sag of -0.7 pu when operating as VSG.

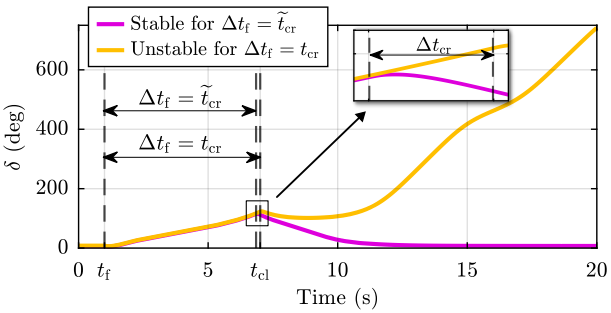

Fig. 8. Virtual angle δ for a symmetrical voltage sag of -0.7 pu when operating as VSG, with $t_{cl} = 5.85$ s in magenta, and $t_{cl} = 6.01$ s in yellow.

Fig. 8. Despite the conservative estimation of $\widetilde{t}_{cr}$, the system responds according to the transient stability assessment within an acceptable deviation of $\Delta t_{cr} = 0.16$ s $\rightarrow \Delta t_{cr} = 2.63\%$.

VSC Results: The same type of fault is applied to observe the system response in the VSC mode. Fig. 9 shows the results in terms of energy, comparing simulated and experimental ones. Note that the energy values behave analogously for the experimental and simulation results. However, the critical energy W_{cr} is lower in the simulation than in the experimental validation. This effect is due to the voltage variation at the PCC, which is included in the analytical model as an algebraic variable V_g, neglecting the dynamic of the filter capacitor C_f, as described in Section II-B.

In the VSC case, the clearing W_{cl} and critical W_{cr} values never intersect, independently of the fault duration, as shown in Fig. 9. According to the stability assessment, this result implies that the VSC is always stable for this type of fault. The VSC stability is confirmed by observing the virtual rotor angle response in Fig. 10. As stated in Section II, the VSC operates at $P_v^* = 0$ pu. Therefore, the virtual rotor does not continue to accelerate during the fault but stops at a stable equilibrium point $\delta_0^f = 23.9°$, explaining why W_{cl} does not increase and is lower than W_{cr}. The stable equilibrium point in the fault condition, δ_0^f, can be analytically calculated by imposing the stationary conditions of the differential equations in (8), with $E_g = E_g^f = 0.3$ pu and $P_v^* = 0$ pu. Therefore, the VSC control reacts to large voltage sag by maintaining its synchronism independently of the fault duration.

Then, the test is conducted with the same clearing time for VSC and VSG modes to compare their transient performance within the stable area. Fig. 11 shows the resulting voltage

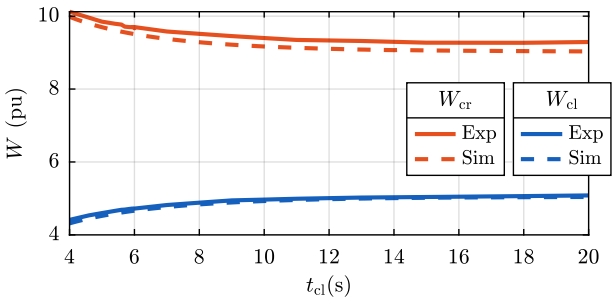

Fig. 9. Critical W_{cr} and clearing W_{cl} values for a symmetrical voltage sag of -0.7 pu when operating as VSC.

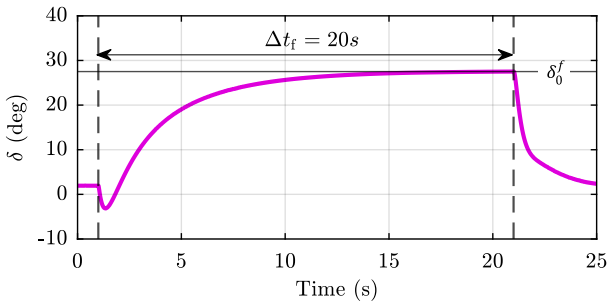

Fig. 10. Virtual angle δ for a symmetrical voltage sag of -0.7 pu when operating as VSC, with $t_{cl} = 20$ s.

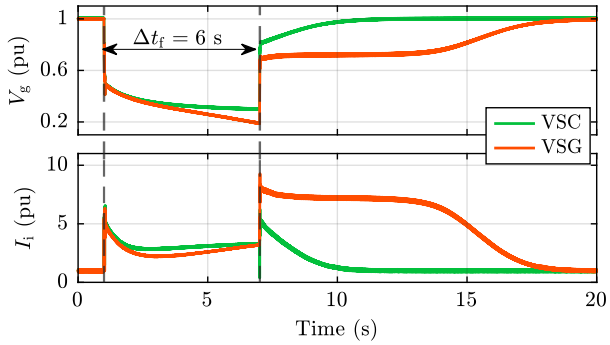

Fig. 11. Voltage amplitude at the PCC V_g and output current amplitude I_i for a symmetrical voltage sag of -0.7 pu operating as VSC in green and VSG in orange, with $t_{cl} = 6$ s.

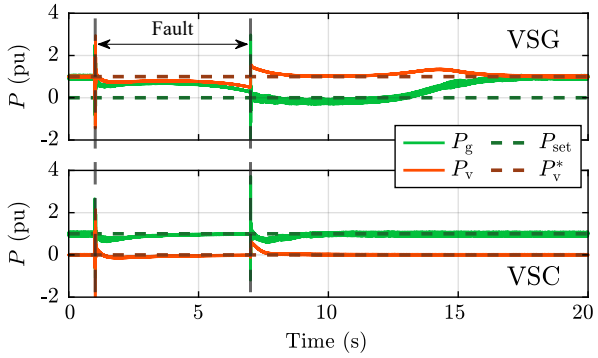

Fig. 12. Active virtual power P_v, active virtual power reference P_v^*, set point reference power P_{set} and grid power P_g for a symmetrical voltage sag of -0.7 pu with $t_{cl} = 6$ s. From top to bottom: VSG operation and VSC operation.

amplitude V_g at the PCC and the output inverter current amplitude I_i. Considering the VSC operation, the output

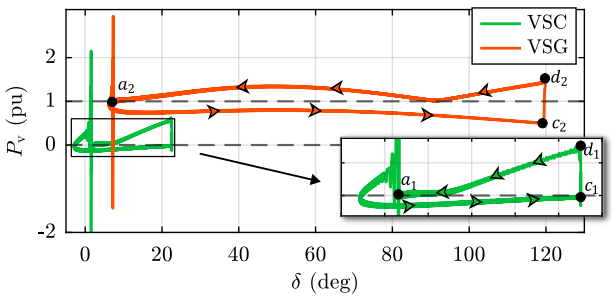

Fig. 13. Active virtual power P_v to the variation of the rotor angle δ for a symmetrical voltage sag of -0.7 pu operating as VSC in green and VSG in orange, with $t_{cl} = 6$ s.

current is the sum of the Power to Current block and the EM part, as presented in Section II. Before the fault occurs in VSC mode, the Power to Current block manages the power exchange by injecting the current $i_i = i_{set} = 1$ pu, whereas $i_v = 0$ pu. At the fault occurrence, the EM part reacts to the system perturbation by injecting the reactive current i_v to support the grid. Therefore, the VSC output current is given by $i_i = i_{set} + i_v$ for $t > t_f$.

For the VSG mode, only the EM block manages the power exchange, thus determining the current injection of $i_i = i_v$. Fig. 12 shows the virtual power P_v with its reference P_v^*, P_{set}, and the grid power P_g to clarify their different roles while operating as VSG and VSC. Considering the VSG operation, the Power to Current block does not operate (i.e., $P_{set} = 0$ pu). Therefore, the virtual P_v and grid power P_g are equal, excepting for the losses in normal operating conditions. During the fault, the virtual power P_v is always lower than the reference P_v^*, thus causing the rotor angle acceleration.

On the other hand, the EM block operates at zero power reference for the VSC, whereas $P_{set} = 1$ pu. When operating as VSC, the virtual P_v and output power P_g differ for the P_{set} injected by the Power to Current block. Note that the EM block rules the VSC transient response. Therefore, the VSC reacts at the fault occurrence according to the EM dynamics, returning to zero virtual power injection during the fault (i.e., $P_v = P_v^*$). As the EM block operates with zero power reference, the VSC can maintain the synchronism even when the grid-tied inverter cannot exchange power with the grid (i.e., short circuit at the point of common coupling).

After the fault clearance, the VSC returns to the pre-fault state (i.e., $I_i = 1$ pu, $V_g = 1$ pu) within 5 s, whereas the VSG within 12 s. The post-fault dynamic can be explained by observing Fig. 13, which shows the control trajectory in the $P - \delta$ frame. When the fault occurs, the VSG cannot provide the reference power, thus determining the rotor acceleration to the point c_2 at 120°. Therefore, the VSG fits case **(b)** presented in Section III. The VSG's post-fault trajectory indeed depends on the clearing time and, in this condition, returns to its pre-fault state. On the other hand, the VSC operates at zero power reference and covers a shorter trajectory toward its new stable equilibrium point c_1 at $P_v = P_v^* = 0$ pu. Therefore, the VSC fits into case **(a)**, hence stable independently of the fault duration. Furthermore, the VSC returns to the pre-fault state faster than the VSG, thanks to the shorter trajectory, thus explaining the different control dynamics in the post-fault.

The VSC response is a significant result, leading toward a new paradigm in the VSM control. The VSC approach indeed combines the SG features (i.e., inertia capability) with the advantages of a fast inverter, determining a control able to:

- Maintain the synchronism during a fault without any additional adjustments, overcoming the limitations of the proposed VSG algorithm modifications available in the literature;
- Provide ancillary services in normal and abnormal operating conditions.

V. Conclusion

This paper demonstrated the benefits of VSC control via a comprehensive transient stability analysis. The transient stability analysis based on Lyapunov's Direct Method is validated experimentally by applying a -0.7 pu voltage sag. In VSG mode, the virtual rotor accelerates during the fault, reaching the instability condition consistently with the transient stability assessment. The same stability analysis was conducted for the VSC operation, showing that the system never reached the unstable condition. The virtual rotor response further supports the analysis results. The VSC reaches a stable equilibrium point during the fault and maintains the synchronism as it operates at zero virtual power reference. Therefore, the VSC mode overcomes the transient stability challenges through its compensator-based control without additional dedicated units or parameter adaptations. Notably, the VSC approach leads to a more advanced VSM-based control capable of providing grid services and maintaining synchronism, even with large voltage sags. Note that this paper does not discuss the current limitation effects on the VSM behaviour but rather demonstrates the operational differences between the VSG and VSC modes. The authors are currently analyzing the effect of the current limitation on the VSG case [29] and will extend the analysis to the VSC case in a dedicated paper. Moreover, the paper considers a system consisting of a grid-tied inverter controlled by a VSM-based algorithm connected to an infinite bus. In the future, the stability analysis will be developed for multi-VSM systems in grid-connected and islanded mode.

Appendix

The virtual admittance Y_v and grid admittance Y_g are defined as in (30). Moreover, the power injection at the PCC is represented as a negative PQ load, as expressed in (31).

$$Y_v = \frac{1}{R_v + jL_v} \quad Y_g = \frac{1}{R_g + jL_g} \tag{30}$$

$$Y_L = \frac{P_{set}}{V_g^2} + j\frac{Q_{set}}{V_g^2} \tag{31}$$

The admittance matrix $\mathbf{Y}$ of the equivalent circuit is the matrix such that:

$$\begin{bmatrix} i_v \\ i_g \end{bmatrix} = \mathbf{Y} \begin{bmatrix} e_v \\ e_g \end{bmatrix} \tag{32}$$

The admittance matrix elements for the power calculation are:

$$\begin{cases} Y_{11} & = Y_{\mathrm{v}} - \dfrac{Y_{\mathrm{v}}^2}{Y_{\mathrm{v}} + Y_{\mathrm{g}} + Y_{\mathrm{g}}} \\ Y_{12} & = -\dfrac{Y_{\mathrm{v}} Y_{\mathrm{g}}}{Y_{\mathrm{v}} + Y_{\mathrm{g}} + Y_{\mathrm{g}}} \end{cases} \tag{33}$$

Therefore, the elements G_{11}, G_{12}, and B_{12} can be calculated as in (34).

$$G_{11} = \mathrm{Re}\left(Y_{11}\right), \quad G_{12} = \mathrm{Re}\left(Y_{12}\right), \quad B_{12} = \mathrm{Im}\left(Y_{12}\right) \tag{34}$$

REFERENCES

[1] U. Tamrakar, D. Shrestha, M. Maharjan, B. P. Bhattarai, T. M. Hansen, and R. Tonkoski, "Virtual inertia: Current trends and future directions," *Applied sciences*, vol. 7, no. 7, p. 654, 2017.

[2] nationalgridESO, "GC0137: Minimum Specification Required for Provision of GB Grid Forming (GBGF) apability (formerly Virtual Synchronous Machine/VSM capability)," Tech. Rep., Mar. 2021.

[3] ENTSO-E, "Frequency Stability in Long-Terms Scenarios and Relevant Requirement," Tech. Rep., Dec. 2021.

[4] Terna, "Code for Transmission Dispatching. Development and Security of the Grid," Grid Code, Mar. 2023.

[5] M. Chen, D. Zhou, and F. Blaabjerg, "Modelling, implementation, and assessment of virtual synchronous generator in power systems," *Journal of Modern Power Systems and Clean Energy*, vol. 8, no. 3, pp. 399–411, 2020.

[6] V. Mallemaci, F. Mandrile, S. Rubino, A. Mazza, E. Carpaneto, and R. Bojoi, "A comprehensive comparison of virtual synchronous generators with focus on virtual inertia and frequency regulation," *Electric Power Systems Research*, vol. 201, p. 107516, 2021.

[7] J. Liu, Y. Miura, and T. Ise, "Comparison of dynamic characteristics between virtual synchronous generator and droop control in inverter-based distributed generators," *IEEE Transactions on Power Electronics*, vol. 31, no. 5, pp. 3600–3611, 2015.

[8] F. Mandrile, E. Carpaneto, and R. Bojoi, "Grid-feeding inverter with simplified virtual synchronous compensator providing grid services and grid support," *IEEE Transactions on Industry Applications*, vol. 57, no. 1, pp. 559–569, 2020.

[9] A.-A. Fouad and V. Vittal, *Power system transient stability analysis using the transient energy function method*. Pearson Education, 1991.

[10] M. Ghandhari, "Control Lyapunov functions: A control strategy for damping of power oscillations in large power systems," Ph.D. dissertation, KTH, 2000.

[11] P. C. Magnusson, "The transient-energy method of calculating stability," *Transactions of the American Institute of Electrical Engineers*, vol. 66, no. 1, pp. 747–755, 1947.

[12] A. H. El-Abiad and K. Nagappan, "Transient stability regions of multimachine power systems," *IEEE Transactions on Power Apparatus and Systems*, no. 2, pp. 169–179, 1966.

[13] T. Qoria, F. Gruson, F. Colas, G. Denis, T. Prevost, and X. Guillaud, "Critical clearing time determination and enhancement of grid-forming converters embedding virtual impedance as current limitation algorithm," *IEEE Journal of Emerging and Selected Topics in Power Electronics*, vol. 8, no. 2, pp. 1050–1061, 2019.

[14] Z. Shuai, C. Shen, X. Liu, Z. Li, and Z. J. Shen, "Transient angle stability of virtual synchronous generators using Lyapunov's direct method," *IEEE Transactions on Smart Grid*, vol. 10, no. 4, pp. 4648–4661, 2018.

[15] M. Chen, D. Zhou, and F. Blaabjerg, "Enhanced transient angle stability control of grid-forming converter based on virtual synchronous generator," *IEEE Transactions on Industrial Electronics*, vol. 69, DOI 10.1109/TIE.2021.3114723, no. 9, pp. 9133–9144, 2022.

[16] L. Latiki, K. Y. Cherif, A. Medjdoub, and N. Taib, "Power systems transient stability assessment via direct method," in *2022 IEEE International Conference on Electrical Sciences and Technologies in Maghreb (CISTEM)*, vol. 4, pp. 1–6. IEEE, 2022.

[17] X. Xiong, C. Wu, and F. Blaabjerg, "Effects of virtual resistance on transient stability of virtual synchronous generators under grid voltage sag," *IEEE Transactions on Industrial Electronics*, vol. 69, DOI 10.1109/TIE.2021.3082055, no. 5, pp. 4754–4764, 2022.

[18] J. Alipoor, Y. Miura, and T. Ise, "Power system stabilization using virtual synchronous generator with alternating moment of inertia," *IEEE journal of Emerging and selected topics in power electronics*, vol. 3, no. 2, pp. 451–458, 2014.

[19] W. Zhao, L. Wang, W. Song, X. Zhang, and Z. Wang, "Variable inertias of wind turbines in interconnected power system for transient stability enhancement," in *2022 IEEE 6th Information Technology and Mechatronics Engineering Conference (ITOEC)*, vol. 6, pp. 812–816, 2022.

[20] M. Li, S. Shu, Y. Wang, P. Yu, Y. Liu, Z. Zhang, W. Hu, and F. Blaabjerg, "Analysis and improvement of large-disturbance stability for grid-connected VSG based on output impedance optimization," *IEEE Transactions on Power Electronics*, vol. 37, no. 8, pp. 9807–9826, 2022.

[21] F. Mandrile, V. Mallemaci, E. Carpaneto, and R. Bojoi, "Lead-lag filter-based damping of virtual synchronous machines," *IEEE Transactions on Industry Applications*, vol. 59, no. 6, pp. 6900–6913, 2023.

[22] F. Mandrile, E. Carpaneto, E. Armando, and R. Bojoi, "Simple tuning method of virtual synchronous generators reactive control," in *2020 IEEE Energy Conversion Congress and Exposition (ECCE)*, pp. 2779–2785. IEEE, 2020.

[23] P. Kundur, *Power system stability*. McGraw-Hill Education, Jan. 1994.

[24] M. Ribbens-Pavella, P. Murthy, and J. Horward, "The acceleration approach to practical stability domain estimation in power systems," in *1981 20th IEEE Conference on Decision and Control including the Symposium on Adaptive Processes*, pp. 471–477. IEEE, 1981.

[25] A.-A. Fouad, V. Vittal, Y.-X. Ni, H. Pota, K. Nodehi, H. Zein-Eldin, E. Vasahedi, and J. Kim, "Direct transient stability assessment with excitation control," *IEEE Transactions on power systems*, vol. 4, no. 1, pp. 75–82, 1989.

[26] P. Ge, C. Tu, F. Xiao, Q. Guo, and J. Gao, "Design-oriented analysis and transient stability enhancement control for a virtual synchronous generator," *IEEE Transactions on Industrial Electronics*, vol. 70, DOI 10.1109/TIE.2022.3172761, no. 3, pp. 2675–2684, 2023.

[27] P. Xie, J. Han, Q. Lu, Y. Dai, Y. Yang, J. Li, Y. Li, and Z. Du, "Transient global stability analysis of virtual synchronous generator," in *2023 8th Asia Conference on Power and Electrical Engineering (ACPEE)*, pp. 285–290. IEEE, 2023.

[28] F. Reißner and G. De Carne, "Virtual synchronous machine integration on a commercial flywheel for frequency grid support," *IEEE Transactions on Power Electronics*, 2024.

[29] A. Camboni, V. Mallemaci, F. Mandrile, and R. Bojoi, "Transient stability improvement of virtual synchronous generators under current limitation: The benefits of virtual power feedback," DOI 10.36227/techrxiv.172684393.35156571/v1, Sep. 2024. [Online]. Available: http://dx.doi.org/10.36227/techrxiv.172684393.35156571/v1

Alessia Camboni (Student Member, IEEE) was born in Sassari, Italy, in 1999. She received the bachelor and master's degrees in electrical engineering in 2020 and 2023, respectively, from the Politecnico di Torino, Torino, Italy, where she is currently working toward the Ph.D. degree with Dipartimento Energia "G. Ferraris". Her Ph.D. topic relates on stability of virtual synchronous machines and control for power electronic grid-connected applications.

Vincenzo Mallemaci (Student Member, IEEE) was born in Messina, Italy, in 1996. He received the bachelor and master's degrees in electrical engineering in 2018 and 2020, respectively, from the Politecnico di Torino, Torino, Italy, where he is also currently working toward the Ph.D. degree with Dipartimento Energia "G. Ferraris". His Ph.D. activity focuses on virtual synchronous machines and control for power electronic grid-connected converters.

Fabio Mandrile (Member, IEEE) received the M.Sc. and Ph.D. degrees in electrical engineering from the Politecnico di Torino, Torino, Italy, in 2017 and 2021, respectively. He is currently an Assistant Professor with Dipartimento Energia ”G. Ferraris”, Politecnico di Torino. His main research interests include virtual synchronous machines and power electronics for grid-connected applications, the experimental characterization of converters, and motor drives.

Radu Bojoi (Fellow, IEEE) received the M.Sc. degree in electrical engineering from the Technical University of Iasi, Iasi, Romania, in 1993, and the Ph.D. degree in electrical engineering from the Politecnico di Torino, Torino, Italy, in 2002. He is currently a Full Professor of power electronics and electrical drives with the Energy Department ”G. Ferraris” and Chairman of the Power Electronics Innovation Center, Politecnico di Torino. He has authored or coauthored more than 200 papers covering electrical drives and power electronics for industrial applications, transportation electrification, power quality, and home appliances. Dr. Bojoi is a past Co-Editor-In-Chief of IEEE TRANSACTIONS ON INDUSTRIAL ELECTRONICS. He was the recipient of six IEEE paper awards. Dr. Bojoi is involved in many research projects with industry aiming at obtaining new products involving emerging technologies.